Nanoscale Res Lett (2010) 5:1190–1194
DOI 10.1007/s11671-010-9624-z

NANO EXPRESS

Pores in *n*-Type InP: A Model System for Electrochemical Pore Etching

Malte Leisner · Jürgen Carstensen · Helmut Föll

Received: 15 April 2010 / Accepted: 28 April 2010 / Published online: 14 May 2010

Abstract The growth mechanism of currentline-oriented pores in *n*-type InP has been studied by Fast-Fourier-Transform Impedance Spectroscopy (FFT IS) applied in situ during pore etching and by theoretical calculations. Several pore growth parameters could thus be extracted in situ that are otherwise not obtainable. These include the space-charge-region (SCR) width, the SCR potential, the capacitance at the pore tips, and the avalanche breakdown field strength. It could be demonstrated that the system adjusts itself in such a way that the potential across the space-charge-region at the pore tips is kept constant within a certain bandwidth of the applied potential. This provides for a constant field strength at the pore tips, ensuring that avalanche breakdown occurs, generating the necessary holes for the electrochemical dissolution of InP.

Keywords Porous semiconductors · InP · Impedance spectroscopy

Introduction

Porous semiconductors have been envisioned for the use in a broad range of applications, and substantial R&D efforts have been made in this direction [1–7]. In the majority of the proposed applications, the detailed morphology of the porous structure is decisive for the functioning of the application. Morphology parameters like pore diameter and shape, pore wall thickness and roughness, or pore density have to be established with often a rather high precision, i.e. for optical applications [4, 8]. To meet precise specifications, a thorough understanding of the pore formation mechanism is needed but not yet established for any pore system, including the thoroughly investigated porous Si. For deeper insights into general pore etching mechanisms, InP can be considered as a model semiconductor, which allows easier systematic investigations than, e.g., Si because only two kinds of pores seem to exist, which are quite different in their general behavior. Changing external parameters like the etching current density or the potential can easily control the respective pore formation modes. Both pore growth modes seem to embody the simplest case of electrochemical pore etching, where only one main electrochemical reaction occurs, in contrast to systems like Si, where always several reactions occur, making the system harder to analyze.

The two pore types present in InP are the so-called crystallographical pores (crystos) and currentline pores (curros). The crysto pores always grow into the <111>B directions of the InP crystal [9, 10], Fig. 1a gives an example. The pores have a triangular cross section and pore tips and grow along the two available "downward" <111> B directions of the crystal ("channels" or lines in the plane of view in Fig. 1a) and into the two available "upward" <111> B directions, intersecting the plane of view in Fig. 1a, giving the appearance of triangular holes.

Figure 1b shows a typical example of curro pores in (100) *n*-type InP [11, 12]. The pores have a circular cross-section and semispherical pore tips. They grow in direction of the current flow, i.e. usually perpendicular to the sample surface, independent of the crystal orientation.

The growth mechanism of crysto pores has already been studied by FFT Impedance Spectroscopy and could be successfully modeled by a stochastic model of the "current burst" type [13], which has been implemented into a

M. Leisner (✉) · J. Carstensen · H. Föll
Institute for Materials Science, Christian-Albrechts-University of Kiel, Kaiserstrasse 2, 24143 Kiel, Germany
e-mail: ml@tf.uni-kiel.de
URL: http://www.tf.uni-kiel.de/matwis/amat/

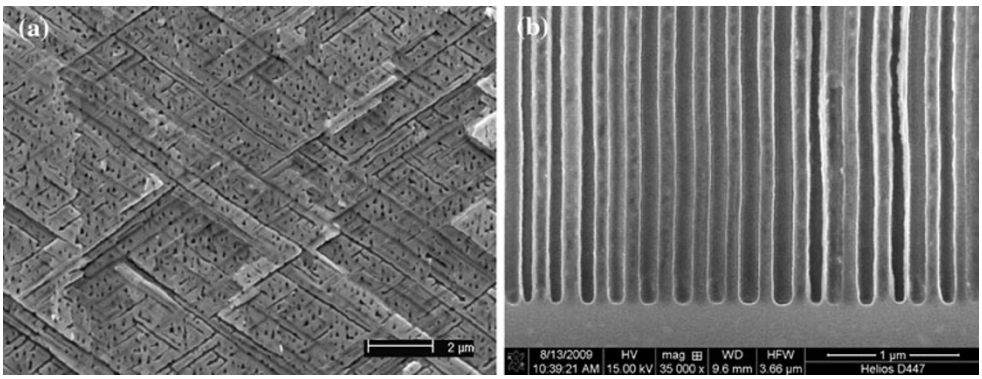

Fig. 1 Cross-sectional view of **a** crystallographical pores in (100) *n*-type InP, **b** currentline pores in (100) *n*-type InP

Monte-Carlo simulation [14, 15]. This work will focus on the growth mechanism behind the currentline pores, expanding the work presented in [16]. Results of the in situ FFT impedance spectroscopy [17] will be analyzed.

Experimental Procedure

All pores have been etched into single-crystalline *n*-type InP wafers. The orientation was (100), and three different doping concentrations N_D have been used: $1{\cdot}10^{17}$, $8{\cdot}10^{17}$, and $3{\cdot}10^{18}$ cm^{-3}. The sample size was $A = 0.25$ cm^2. The samples have been etched in an electrochemical double cell, the basic set-up is described in detail in [18]. 6 wt% HCl aq. has been used as electrolyte. All experiments have been conducted at $T = 20°C$ under constant etching potential. The dc potential used was in the range of 6–8 V for $N_D = 1{\cdot}10^{17}$ cm^{-3}, 4–7 V for $N_D = 8{\cdot}10^{17}$ cm^{-3}, and 2–4 V for $N_D = 3{\cdot}10^{18}$ cm^{-3}. In these potential ranges "good quality" pores can be obtained, i.e. pores with straight and smooth pore walls, growing perpendicular to the surface. In the beginning of the experiments, a high-potential pulse has been applied for 1 s to guarantee a homogeneous nucleation of the pores. Typical etching times were between 5 and 70 min, resulting in pore depths up to 500 µm, i.e. aspect ratios of >1,000.

During all experiments, FFT impedance spectra (FFT IS) [17, 19] were recorded every 1.5 s. The measurement signal contained 28 frequencies between 30 Hz and 20 kHz. The spectra obtained were fitted to a model, which allowed on-line extraction of the model parameters.

Results

Regular arrays of currentline pores can be etched into InP for all three doping concentrations investigated. Figure 2a–c shows cross-sectional SEM images of typical pore structures. It can be seen that the pores grow perpendicular to the surface and have a fairly round tip, which gets slightly flatter with increasing N_D (see the insets). The pore diameter $w_{pore} = 130$ nm is pretty much the same in all cases and thus can be seen as being independent of the doping concentrations and of the etching potentials used as long as they are inside the potential ranges for good quality pores. The pore wall thickness d_{wall}, on the other hand, strongly depends on the doping concentration N_D; it decreases with increasing N_D. As is already known from the literature [20], an analysis of the top view of pores showed that these pores grow in a self-organized hexagonal lattice.

Figure 2d–f shows typical FFT IS spectra recorded during the etching for the three respective doping concentrations shown in a–c after 38 min of etching. The dots represent the measured data, which were fitted (line) by

$$Z(\omega) = R_S + \frac{R_1}{1 + i\omega R_1 C_1} + \frac{R_2}{1 + (1+i)\sqrt{\omega\tau_2}} + \frac{R_3}{1 + i\omega R_3 C_3}, \quad (1)$$

where $Z(\omega)$ is the model impedance, R_S is a serial resistance, R_1, R_2, and R_3 are transfer resistances, C_1 and C_3 are capacitances, and τ_2 is a time constant. The measurement frequencies are indicated in the graphs. It can be seen that Eq. 1 is able to fit the data for all three doping concentrations very well, even though the absolute numbers on the axes are quite different between the experiments. It should be mentioned that the fit is just as good to the 500–2,800 FFT IS obtained through one etching experiment after the short nucleation phase (<1 min), lending credibility to the model used. The amount of data generated will easily exceed the page limitation of any publication, in what follows we will therefore focus on some selected aspects of the model that yield the deepest insights into the pore etching mechanisms.

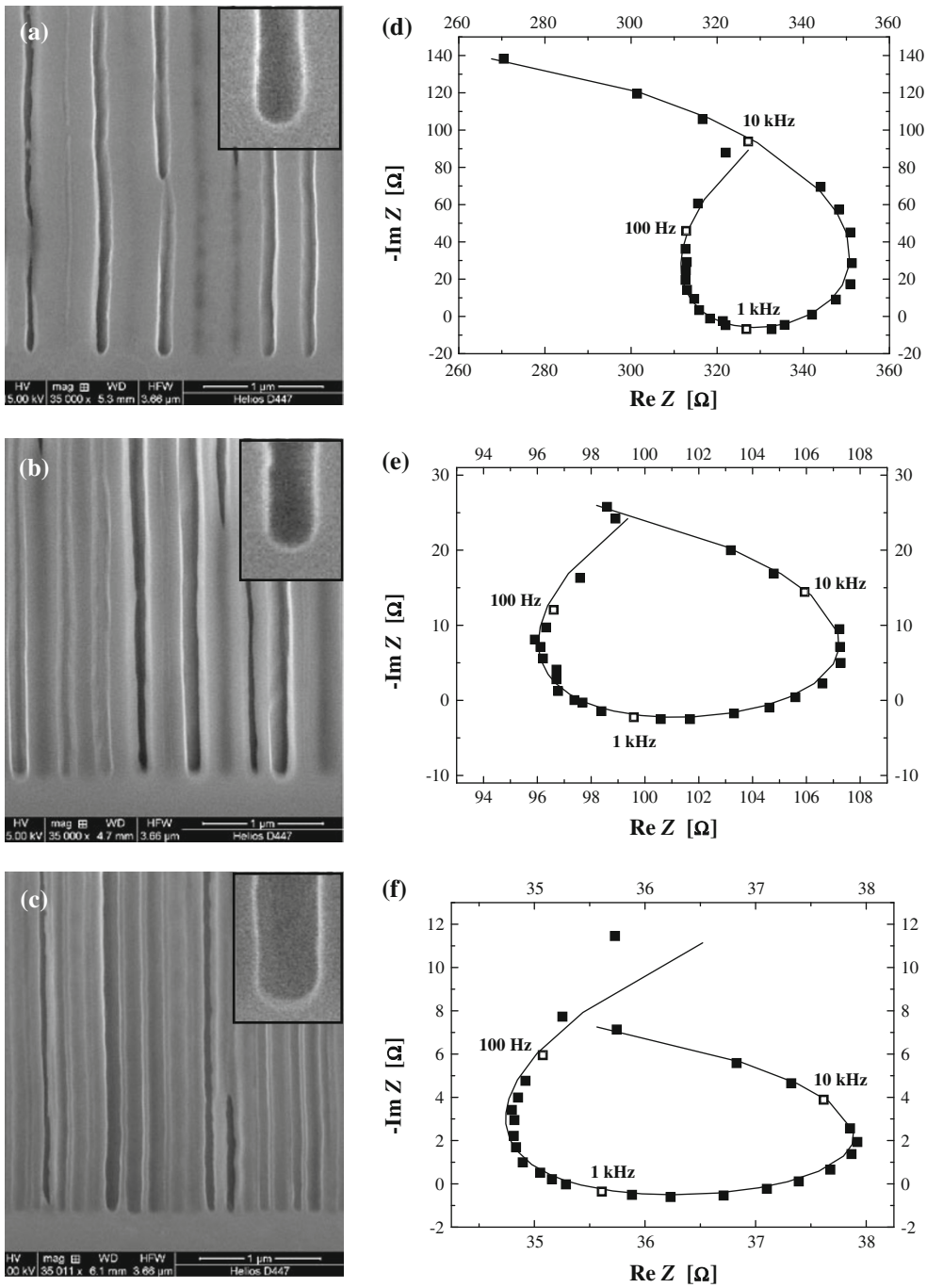

Fig. 2 Cross-sectional SEM images of curro pores etched into (100) *n*-type InP. **a** $N_D = 1{\cdot}10^{17}$ cm^{-3}, $U = 7$ V, **b** $N_D = 8{\cdot}10^{17}$ cm^{-3}, $U = 5.5$ V, **c** $N_D = 3{\cdot}10^{18}$ cm^{-3}, $U = 3$ V. A magnified view of the pore tips is shown in the *insets*. In **d**, **e**, and **f** a typical FFT IS spectrum is shown in form of a Nyquist plot recorded after 38 min of etching. The points represent the measured data, the line is calculated by fitting the measurements to the model given in Eq. 1. The measurement frequencies are indicated

Discussion

Figure 3 shows the product of the etching current I with $R_1 + R_2$ as measured by FFT IS, which has the units of a voltage (or potential). Shown are several curves for each doping concentration, which correspond to experiments with different etching potentials in the aforementioned etching potential window that yielded good quality pores. The I $(R_1 + R_2)$ curves are independent of the etching potential, only depend on the doping concentration N_D, and are essentially constant after an initial nucleation phase. In the nucleation phase, the pores do not yet grow in the close-packed hexagonal geometry, and thus the active area differs and affects R_1 and R_2; therefore, I $(R_1 + R_2)$ deviates from the constant value in this range. It is tempting to assume that the product I $(R_1 + R_2)$: $= U_{SCR}$ is the potential drop over the space-charge-region (SCR) and in what follows we will argue that this is indeed the case. R_1

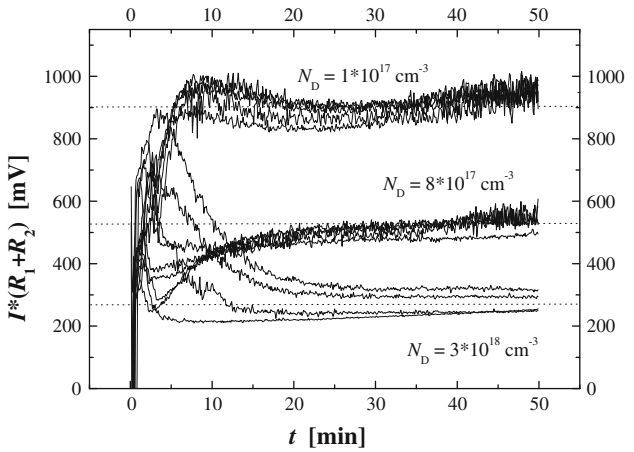

Fig. 3 Potential drop $U_{SCR} := I\ (R_1 + R_2)$ over the space-charge-region (SCR). Several lines correspond to different etching potentials in the aforementioned respective etching potential windows. The *curves* are constant after an initial nucleation phase and dependent on N_D

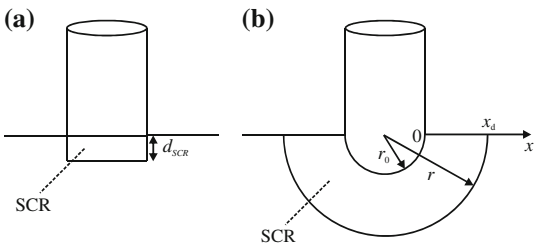

Fig. 4 Geometries used for theoretical calculations of the SCR properties. **a** Planar geometry. **b** Semi-spherical geometry

and C_1 must then be interpreted as the resistance and capacitance of the SCR, while R_2 and τ_2 represent the avalanche breakdown mechanism, which is generating the holes required to etch the semiconductor anodically.

To prove our claim, we have calculated U_{SCR} as a function of doping and pore tip geometry. To do this, the pore geometry (hexagonal lattice arrangement, pore diameter, pore wall thickness) has to be known to some extent, and these values have been determined by SEM. To obtain the properties of the SCR, the Poisson equation has to be solved, yielding the SCR thickness, capacitance and field strength at the pore tips. This is a standard textbook problem for the planar geometry as illustrated in Fig. 4a, cf. [21]. Pore walls need not to be considered, since (by definition) no appreciable current flows through pore walls. For a semi-spherical geometry, as presented in Fig. 4b, a solution of the Poisson equation is given in [22]. These two geometries describe the extremes for the real pore tip shape, which lies between the perfect semi-spherical geometry and the planar geometry, dependent on N_D, as shown in the insets of Fig. 2. For all calculations, U_{SCR}, as described in Fig. 3, serves as input parameter.

Table 1 Pore wall thickness d_{wall} as measured from Fig. 2 is in good agreement with twice the value of the SCR width d_{SCR}, which has been calculated for * planar geometry and ** semispherical geometry

N_D/cm^{-3}	d_{wall}/nm measured	2 d_{SCR}/nm* calculated	2 d_{SCR}/nm** calculated
$1{\cdot}10^{17}$	148	230	168
$8{\cdot}10^{17}$	94	62	55
$3{\cdot}10^{18}$	27	22	21

The thickness of the SCR has been calculated for both geometries and for all three doping concentrations; it is tabulated in Table 1. It is given as 2 d_{SCR}, since it is commonly expected that the pore wall thickness is defined by twice the distance of the space-charge-region, leading to an overlap of the SCRs and thus insulating pore walls, which cannot be further electrochemically dissolved, since no holes are present. Table 1 therefore also shows the pore wall thickness d_{wall}, as measured by SEM. It can be seen that the values are in good agreement, and that the N_D dependence is correct.

The capacitance of the SCR at the pore tips C_{SCR} can be calculated analogously for both geometries. Figure 5 shows the calculated values for the planar (boxes) and semi-spherical (circles) geometry. The stars represent the data measured by FFT IS (C_1). It can be seen that these values always lie in between the boundaries that describe the two extreme geometries. Furthermore, the values move to the planar boundary with increasing N_D. This reflects very well the change in pore tip shape from round to flat with increasing N_D, which is visible in the insets of Fig. 2.

The last SCR quantity that has been calculated is the field strength at the pore tips E_{calc}. The calculated values

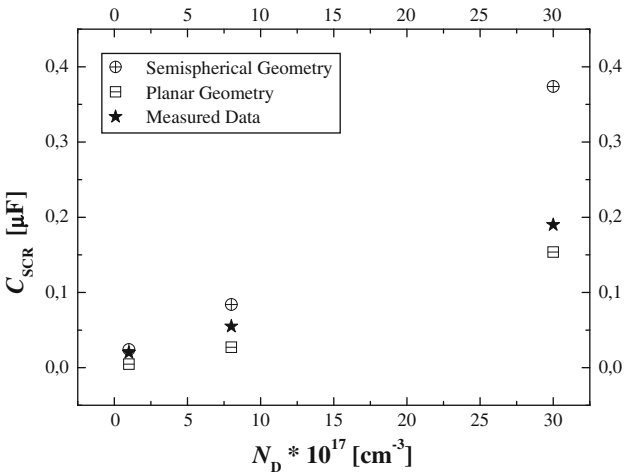

Fig. 5 Capacitance of the SCR at the pore tips C_{SCR}. The *squares* represent the values calculated for the planar boundary, the *circles* the values for the semi-spherical boundary. The *stars* represent the capacitance C_1, as measured by FFT IS

Table 2 Potential drop in the SCR, U_{SCR}, and field strength at the pore tips E_{calc}, as calculated from the FFT IS data

N_D/cm^{-3}	U_{SCR}/mV	E_{calc} Vcm^{-1}	E_m Vcm^{-1}
$1{\cdot}10^{17}$	956	350.000	648.000
$8{\cdot}10^{17}$	553	470.000	840.000
$3{\cdot}10^{18}$	272	540.000	991.000

For comparison, the maximum field strength E_m for avalanche breakdown, according to Eq. 2, is also given

are listed in Table 2. These values are compared to theoretical values of the maximum field strength E_m for avalanche breakdown, which can be calculated after [21, 23] by

$$E_m = \left(\frac{E_g}{1.1\,\mathrm{eV}}\right)^{3/4} \varepsilon_r^{1/2} \left(\frac{N_D}{10^{17}\mathrm{cm}^{-3}}\right)^{1/8} 1.96\,\mathrm{V/cm}, \qquad (2)$$

where E_g is the bandgap and ε_r the dielectric constant of the semiconductor. Please note that the values of E_m are for an all solid InP pn-junction, the best comparison available, since no data for the InP-HCl junction exists. Nevertheless, Table 2 shows that the values are in good agreement with E_{calc}, as calculated by FFT IS.

This last finding supports the fact that the part of the impedance described by R_2 and τ_2 is the avalanche breakdown mechanism, indeed. This interpretation is also capable of explaining the negative (differential) impedance, i.e. the "inductive" loop, which is always present.

All things considered, the results strongly support the validity of the model expressed in Eq. 1 and the interpretation of parameters extracted.

We believe that the third process represents the diffuse layer inside the pores, where R_3 and C_3 describe the respective resistance and capacitance. This claim has not yet been supported by theoretical calculations, but might yield further insights in the near future.

Conclusion

It has been demonstrated that currentline pore growth in InP is governed by a constant potential U_{SCR} in the SCR, which keeps the field strength required for avalanche breakdown constant (since the pore tip shape does not change). This mechanism is present at all three investigated doping concentrations N_D, for which hexagonally close packed pore structures with different pore wall thicknesses, but constant pore diameter have been observed. It was possible to extract several important parameters for the etching process in situ, which are otherwise not obtainable. These include the SCR width, the SCR potential, the capacitance at the pore tips, and the avalanche breakdown field strength.

References

1. V. Lehmann, *Electrochemistry of silicon* (Wiley-VCH, Weinheim, 2002)
2. H. Föll, M. Leisner, A. Cojocaru, J. Carstensen, Materials, accepted for publication
3. V. Kochergin, H. Föll, *Porous semiconductors: optical properties and applications* (Springer, London, 2009)
4. M.J. Sailor, *Porous silicon in practice: preparation* (Characterization and Applications, Wiley-VCH, 2010)
5. J.-N. Chazalviel, F. Ozanam, Macropores in p-type silicon, in *Ordered porous nanostructures and applications*, ed. by R.B. Wehrspohn (Springer, Berlin, 2005)
6. S. Ossicini, L. Pavesi, F. Priolo, *Light emitting silicon for microphotonics* (Springer, Berlin, 2003)
7. A. Sa′ar, J. Nanophoton. 3, 032501 (2009)
8. V. Kochergin, H. Föll, Mater. Sci. Eng. R **52**(4–6), 93 (2006)
9. H. Föll, S. Langa, J. Carstensen, S. Lölkes, M. Christophersen, I.M. Tiginyanu, Adv. Mater. **15**, 3–183 (2003)
10. T. Takizawa, S. Arai, M. Nakahara, Japan J. Appl. Phys. **33**(2, 5A), L643 (1994)
11. H. Föll, S. Langa, J. Carstensen, M. Christophersen, I.M. Tiginyanu, III-Vs Review **16**(7), 42 (2003)
12. E. Kikuno, M. Amiotti, T. Takizawa, S. Arai, Japan J. Appl. Phys. **34**(1, 1), 177 (1995)
13. J. Carstensen, R. Prange, G.S. Popkirov, H. Föll, Appl. Phys. A **67**(4), 459 (1998)
14. M. Leisner, J. Carstensen, A. Cojocaru, H. Föll, ECS Trans. **16**(3), 133 (2008)
15. M. Leisner, J. Carstensen, H. Föll, ECS Trans. **19**(3), 321 (2009)
16. M. Leisner, J. Carstensen, A. Cojocaru, H. Föll, Phys. Stat. Sol. (c) **206**, 7–1566 (2009)
17. G.S. Popkirov, R.N. Schindler, Rev. Sci. Instrum. **63**, 5366 (1992)
18. S. Langa, I.M. Tiginyanu, J. Carstensen, M. Christophersen, H. Föll, Electrochem. Solid-State Lett. **3**(11), 514 (2000)
19. J. Carstensen, E. Foca, S. Keipert, H. Föll, M. Leisner, A. Cojocaru, Phys. Stat. Sol. (a) **205**, 11–2485 (2008)
20. S. Langa, I.M. Tiginyanu, J. Carstensen, M. Christophersen, H. Föll, Appl. Phys. Lett. **82**, 2–278 (2003)
21. S.M. Sze, *Physics of semiconductor devices* (Wiley & Sons, New York, 1981)
22. X.G. Zhang, J. Electrochem. Soc. **138**, 3750 (1991)
23. S.M. Sze, G. Gibbons, Appl. Phys. Lett. **8**, 5–111 (1966)